Quantitative x-ray photoelectron spectroscopy study of Al/AlO_x bilayers

Xavier Batlle,[a] Bart Jan Hattink, and Amílcar Labarta
Departament Física Fonamental, Universitat Barcelona, Diagonal 647, 08028, Barcelona, Catalonia, Spain

Johan J. Åkerman, Roberto Escudero,[b] and Ivan K. Schuller
Department of Physics, 0319, University of California, San Diego, 9500 Gilman Drive, La Jolla, California 92093

(Received 26 November 2001; accepted for publication 22 March 2002)

An x-ray photoelectron spectroscopy (XPS) analysis of Nb/Al wedge bilayers, oxidized by both plasma and natural oxidation, is reported. The main goal is to show that the oxidation state—i.e., O:(oxidize)Al ratio—, structure and thickness of the surface oxide layer, as well as the thickness of the metallic Al leftover, as functions of the oxidation procedure, can be quantitatively evaluated from the XPS spectra. This is relevant to the detailed characterization of the insulating barriers in (magnetic) tunnel junctions. © *2002 American Institute of Physics.* [DOI: 10.1063/1.1478791]

I. INTRODUCTION

Recently, considerable effort has been devoted to the study of magnetic tunnel junctions (MTJs). These exhibit high-tunneling magnetoresistance (TMR),[1–2] and can potentially be applied to magnetic-field sensors,[3] magnetic random access memories (MRAM),[4–6] and read-head applications.[7–8] MTJs have a basic FM/I/FM structure, where FM are ferromagnetic electrodes and I is an insulating barrier of $\sim$1–2 nm in thickness. Most of the research has been undertaken on insulating barriers based on an Al layer which is oxidized after being deposited by either natural oxidation in air,[1] plasma oxidation (oxygen glow discharge),[2,9–14] or oxidation in pure oxygen.[14] Although the first room-temperature junctions were prepared using natural oxidation of Al in air,[1] it was soon found that plasma oxidation is more reliable for MTJs with high TMR.[2] Other oxidation strategies, such as ultraviolet-light-assisted oxidation,[15–16] also achieve high-TMR values.

MTJs with TMR above about 40% at room temperature and adjustable resistance-area products $R\times A$ from 10^6 $\Omega\,\mu m^2$ to a few hundred $\Omega\,\mu m^2$ can now be obtained,[17–18] which makes them suitable for MRAM applications. However, thermal stability up to $\sim$400–450 °C is required to cope with the standard backend process occurring during MTJ integration with a complentary metal-oxide-semiconductor wafer,[5] while the TMR signal usually decreases above 300 °C due to the polarization loss of the CoFe top electrode caused by Mn (in Mn-X exchange layer) diffusion from the pinning layer.[10–11] Recently, thermal stability has been improved up to $\sim$380 °C (TMR=39%)[19–21] by the insertion of an FeO_x layer of appropriate thickness between the insulating AlO_x barrier and the top pinned FM electrode. Low-resistance MTJs are also potential candidates for replacement of spin-valve sensors in read heads, as recording densities move beyond 100 Gbit/inch^2, provided $R\times A$ is of the order of a few $\Omega\,\mu m^2$ and TMR $\sim$20%. Two basic strategies are followed to meet these requirements: (i) thinner AlO_x barriers (5 to 7 Å Al),[22] and (ii) lower band-gap oxides, ZrO_x and HfO_x among others, as barriers.[23]

The performance of the junctions is strongly dependent on the oxidation of the FM electrodes at the FM/I interfaces.[24–25] It also depends on the oxidation state of the barrier, which has to be homogenous and complete (no metallic Al leftover). The use of thinner and thinner barriers has also reopened the question of how to rule out the presence of pinholes (direct metal-to-metal microshorts). The recent observation of very high-ballistic magnetoresistance (MR) up to 300% in magnetic nanocontacts[26–29] suggests that pinholes might enhance the device performance by simultaneously contributing to its high MR and low $R\times A$. Rowell and others developed during the 1960s a set of criteria to ascertain that tunneling is the dominant mechanism in junctions with at least one superconducting (S) electrode.[30] Three of these criteria are still used in FM/I/FM structures: (i) an exponential insulator thickness (t) dependence of the conductance, $G(t)$; (ii) a quasiparabolic voltage (V) dependence of G; and (iii) a weak insulatinglike temperature dependence $G(T)$; though (i) and (ii) have recently been shown to be unreliable.[31–32] For the third criterion, some results suggest that pinholes yield a metalliclike temperature dependence of the junction resistance.[32–33] Therefore, out of the three Rowell criteria, only one, the insulatinglike $G(T)$, seems to be still reliable. Recently, some of us have proposed a set of quality criteria for the identification of barrier shorts in MTJs.[34]

X-ray photoelectron spectroscopy (XPS)[35–36] is an excellent technique for the analysis of thin insulating barriers.[14,20–21,23–25,37–40] In XPS, in-coming monochromatic x-rays are used to eject electrons from the sample. These are collected and the binding energy of their atomic core level is inferred from their kinetic energy. XPS has an energy resolution that permits study of the chemical species in the sample as well as the bonding state (either metallic or insu-

[a]Author to whom correspondence should be addressed; electronic mail: xavier@ffn.ub.es
[b]Permanent address: IIM-UNAM, Mexico City, D.F. Apartado Postal 70-360, Mexico.

 © 2002 American Institute of Physics

Downloaded 08 Jun 2010 to 161.116.168.169. Redistribution subject to AIP license or copyright; see http://jap.aip.org/jap/copyright.jsp

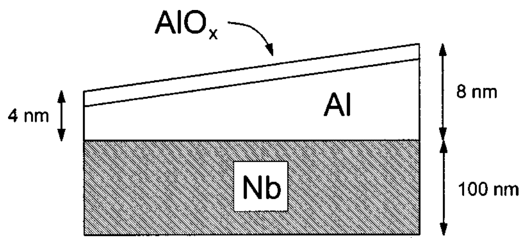

FIG. 1. Bilayer structure of the Nb/Al wedges.

lating) of a given element. This is suitable for the analysis of, for example, the relative AlO_x-Al ratio, which governs the transport properties of MTJs. As the XPS signal is proportional to the number of out-coming photoelectrons per second reaching the detector from a region about a few nanometers below the surface–i.e., from a distance equivalent to about three times the inelastic mean free path λ-the sample is usually ion-beam sputtered at low energy in order to gain a depth profile.[35] XPS has proved it can characterize the oxidation state at tunnel junction interfaces[24–25] and analyze the performance of a variety of insulating barriers (AlO_x, $AlZrO_x$, $AlHfO_x$)[23,40] as a function of both the oxidation conditions and annealing strategies, down to a total barrier thickness of 7 Å (low-resistance junctions). XPS has also suggested that oxygen migration from the FeO_x inserted layer to the AlO_x insulating barrier is responsible for the enhancement of thermal stability.[20–21]

This paper reports a quantitative XPS analysis of Nb/Al wedge bilayers, oxidized by both plasma and natural oxidation. The main goal is to show that the oxidation state–i.e. O:(oxidize)Al ratio–, structure and thickness of the surface oxide layer, as well as the thickness of the metallic Al leftover, as functions of the oxidation procedure, can be quantitatively evaluated from the XPS spectra. This is relevant to the detailed characterization of the insulating barriers in MTJs, since, although XPS has been used qualitatively for the analysis of these, there is not much quantitative information in the literature.

II. EXPERIMENT

Nb (100 nm)/Al bilayers were dc sputtered onto Si substrates. The base pressure was 1.0×10^{-7} torr. The nominal thickness of the wedge Al layer, t_{Al}, (Fig. 1) ranged from 4 nm (thinnest area) to 8 nm (thickest area). The Al wedge was much thicker than the Al layers used in actual FM/I/FM junctions,[1–2,9–21] in order to get a separation between the AlO_x and Al layers in the XPS spectra. The deposition of the Al wedge started immediately after the deposition of the Nb layer was finished, in order to avoid any interface oxidation due to the oxygen remaining in the chamber.[25] The wedge was made by positioning the substrate off center but still parallel to the surface of the target. Sample W_{AIR} was exposed to ambient air for about two months. Sample W_{PLASMA} was glow discharged ($p_{O2}=350$ m Torr, 350 V dc bias) for 2.3 h. These conditions were chosen to ensure saturation of the Al oxide growth for both methods. The XPS spectra for the O 1s, Nb 3$d_{5/2}$, and 3$d_{3/2}$, Al 2p, C 1s, and Ar 2$p_{3/2}$, and 2$p_{1/2}$ core levels were recorded using the Al K_α emission line ($h\nu=1486.6$ eV; incident angle of the beam: 45°) at a base pressure of 5.0×10^{-10} torr, for W_{AIR} and W_{PLASMA} in both the thinnest and thickest areas of the wedge. We will refer to them as $W_{AIR}(t_{Al}=4$ nm), $W_{AIR}(t_{Al}=8$ nm), $W_{PLASMA}(t_{Al}=4$ nm) and $W_{PLASMA}(t_A=8$ nm). Depth profiles were obtained by an *in situ* low-energy (4 keV, incident at 45°) sputtering process with a step of 18 s, as follows:[35] step 1 is the XPS surface spectrum, step 2 is the XPS spectrum after sputtering for 18 s, so that step n is the XPS spectrum after sputtering for $18(n-1)$ s. This etching process (ca. 5–10 nm per minute), together with the fact that XPS has a probing depth about 5–10 nm, precludes the observation of sharp interfaces and reduces spatial resolution. Energy calibration was performed by adopting the C 1s core level associated with the usual surface contamination layer (binding energy $E_B=284.8$ eV), as reference peak.[35] The latter procedure was also checked by the Ar 2$p_{3/2}$ core level, which is related to ion implantation during the low-energy etching process.

III. RESULTS

Figures 2(a), 2(b), and 2(c) show the XPS spectra for ($Al+AlO_x$) 2p, O 1s, and Nb 3$d_{5/2}$ and 3$d_{3/2}$ core levels, respectively, for sample $W_{AIR}(t_{Al}=8$ nm). Numbers indicate the sputtering step. The main general results are the following: (i) no Nb-O compound is detectable for any sample; (ii) there is always a metallic Al leftover for all samples, as expected from the former Al thickness; typical values of the thickness of the AlO_x barrier obtained from transport measurements[9,12,32] and high-resolution electron microscopy[12,41] of MTJs lay within 1–3 nm depending on the oxidation conditions; and (iii) some Ar implantation becomes clear with increased sputtering time.

From the experimental intensity (total area) of an XPS peak associated with a given core level of an element j, $I(j)$, the atomic fraction of that element in the sample, $C(j)$, may be estimated as:[35–36]

$$C(j)=[I(j)/SF(j)]/[\Sigma_j I(j)/SF(j)], \quad (1)$$

where $SF(j)$ are the atomic sensitivity factors for XPS, which are tabulated for most of the chemical elements and are directly proportional to the product of the scattering cross-section σ times the inelastic mean free path λ associated with a given photoelectron core level.[35–36] Figure 3(a) shows the atomic concentration obtained from the XPS intensities [Eq. (1)] for ($Al+AlO_x$), O, Nb, C, and Ar, as a function of the sputtering step (and time), for sample $W_{PLASMA}(t_{Al}=8$ nm). Figure 3(b) shows a typical fitting of the intensities of the Al and AlO_x contributions to the (Al $+AlO_x$) 2p spectra. The oxide contribution shows the characteristic symmetric peak, while the metallic one is asymmetric due to the small-energy electron-hole excitations near the Fermi level.[35] Figures 4 and 5 show the depth profiles obtained from the fitted Al and AlO_x contributions, for all four samples.

Downloaded 08 Jun 2010 to 161.116.168.169. Redistribution subject to AIP license or copyright; see http://jap.aip.org/jap/copyright.jsp

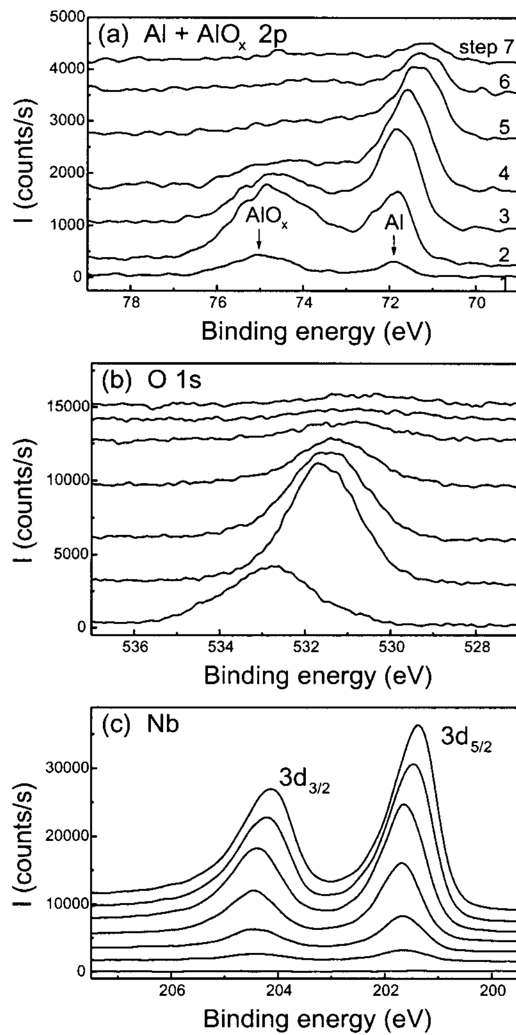

FIG. 2. Sample W_{AIR} ($t_{Al}=8$ nm): (a) XPS spectra for the $(Al+AlO_x)$ $2p$ core level, (b) O $1s$ core level, and (c) Nb $(3d_{5/2}+3d_{3/2})$ core levels. Numbers in (a) indicate the sputtering step. Spectra shown in (b) and (c) correspond to exactly the same steps as in (a) [from bottom to top].

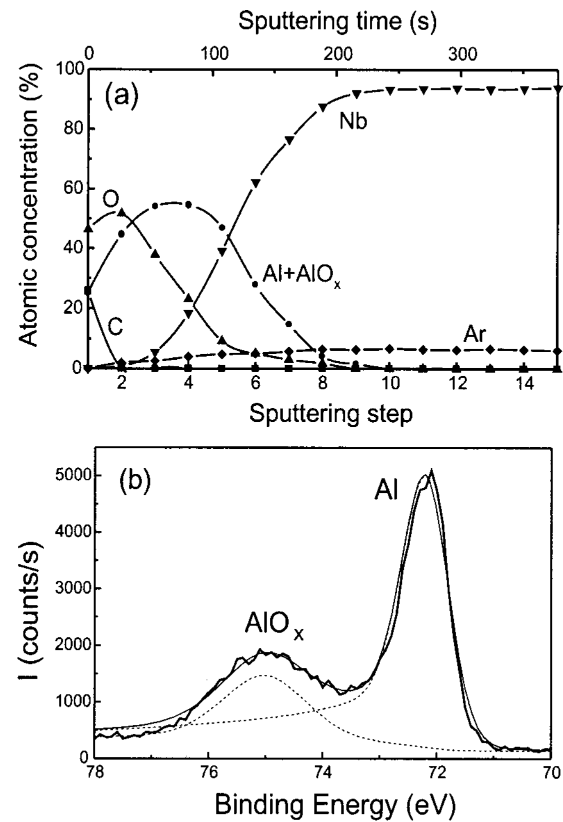

FIG. 3. (a) Sample W_{PLASMA} ($t_{Al}=8$ nm): Atomic concentration obtained from the XPS intensities for $(Al+AlO_x)$, O, Nb, C, and Ar, as a function of sputtering step (and time). (b) Typical fitting of the intensities of the Al and AlO_x contributions to the $(Al+AlO_x)$ $2p$ spectra.

IV. DISCUSSION

The quantitative relation between the XPS intensity I (number of photoelectrons per second in a specific peak of the spectra) and the concentration C (number of atoms per cm^3) of a given element that is distributed throughout a sample of nominal thickness d can be described by an explicit function of the photoelectron escape depth, which is written, omitting some parameters that depend on the experimental setup (e.g., illuminated area, x-ray flux, detector efficiency), as proportional to[35–36]

$$I \propto (\lambda \cos\theta)^{-1} SF \int_0^d C(z) \exp[-z/(\lambda\cos\theta)]dz, \qquad (2)$$

where $C(z)$ is the local concentration at depth z from the surface of the sample, and $\cos\theta$ is a geometrical factor arising from the detector being placed at an angle θ from the normal to the sample surface (take-off angle; $\theta=45°$ in our experimental setup). The exponential factor $\exp[-z/(\lambda\cos\theta)]$ measures the decay in the number of electrons per second that reach the detector due to inelastic scattering within the sample. XPS thus samples the element distribution within a distance about $3\lambda\cos\theta$ below the surface.

By assuming that in the present Nb/Al wedges, a homogenous AlO_x layer of thickness t_{ox} has grown on top of a homogenous, metallic Al leftover of thickness d_{Al}, Eq. (2) leads to

$$I(AlO_x)/I(Al) = [\rho(AlO_x)/\rho(Al)][A(Al)/A(AlO_x)] \times [\exp(t_{ox}/(\lambda_{Al}\cos\theta)) - 1], \qquad (3)$$

where $\rho(AlO_x)$ and $\rho(Al)$, and $A(AlO_x)$ and $A(Al)$, are the mass densities and atomic weights of the oxide and metallic Al phases, respectively. Consequently, t_{ox} may be quantitatively evaluated as

$$t_{ox} = \lambda_{Al}\cos\theta \ln(R/K+1), \qquad (4)$$

where the inelastic mean free path for Al $2p$ electrons λ_{Al} may be estimated as $\lambda_{Al} \approx 3\times[K_E/1386.6]^{0.72} \approx 3.04$ nm,[35–36] K_E being the kinetic energy ($K_E = h\nu - E_B$; $E_B \approx 72.5-72.9$ eV is the expected binding energy Al $2p$ electrons in metallic Al), $R = I(AlO_x)/I(Al)$ being the intensity ratio of oxidized-to-metallic Al in step 1 (surface spectrum), and $K = [\rho(AlO_x)A(Al)]/[\rho(Al)A(AlO_x)]$ being the ratio of atomic densities. The above expression for λ as a function of K_E stands for a phenomenological law that applies to a wide variety of elements.[35] Equations (3) and (4) apply, provided that $\exp[-t_{Al}/(\lambda_{Al}\cos\theta)] \ll 1$, i.e., when the upper limit in the integral for $I(Al)$ in Eq. (2) may be substituted by ∞.

Downloaded 08 Jun 2010 to 161.116.168.169. Redistribution subject to AIP license or copyright; see http://jap.aip.org/jap/copyright.jsp

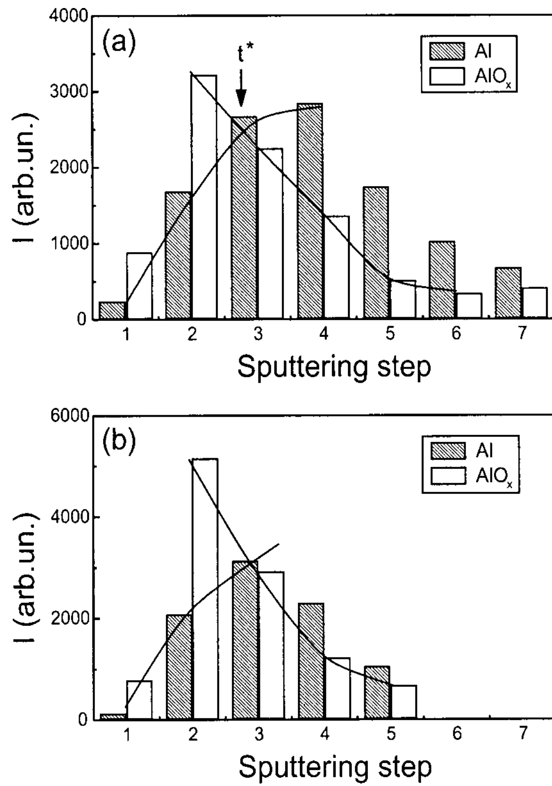

FIG. 4. Depth profile showing the fitted intensities of the Al and AlO_x contributions to the $(Al+AlO_x)$ $2p$ spectra, for samples (a) W_{AIR} ($t_{Al}=8$ nm) and (b) W_{AIR} ($t_{Al}=4$ nm). t^* indicates the sputtering time for which $I(AlO_x)=I(Al)$. Solids lines—intensity as a function of sputtering step—are a guide for the eyes.

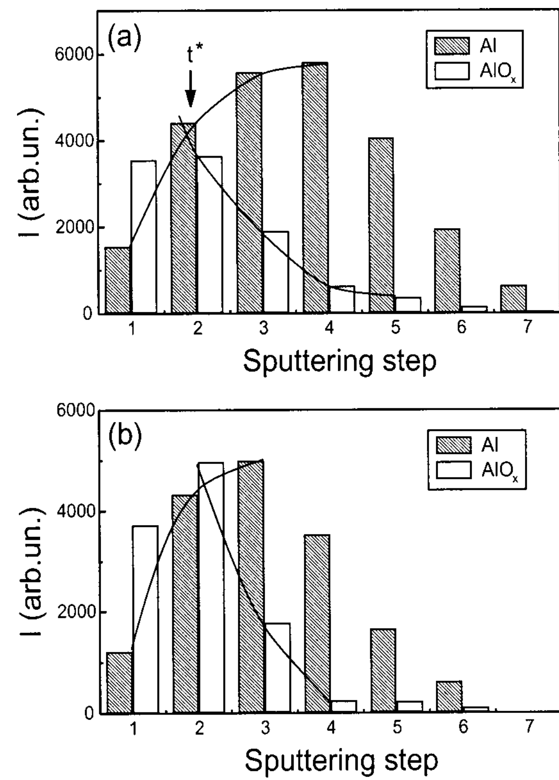

FIG. 5. Depth profile showing the fitted intensities of the Al and AlO_x contributions to the $(Al+AlO_x)$ $2p$ spectra, for samples (a) W_{PLASMA} ($t_{Al}=8$ nm) and (b) W_{PLASMA} ($t_{Al}=4$ nm). t^* indicates the sputtering time for which $I(AlO_x)=I(Al)$. Solids lines—intensity as a function of sputtering step—are a guide for the eyes.

This is the case for those two samples with $t_{Al}=8$ nm (thickest area of the wedge) and the latter inequality indicates that the nominal thickness of the former Al layer must be much larger than λ_{Al}. Experimental support to this assumption is given by the fact that no Nb signal is detected in step 1 when the spectra are taken in the thickest area of the wedge. Equation (4) yields $t_{ox}=2.4$ nm for W_{AIR} ($t_{Al}=8$ nm) and $t_{ox}=1.8$ nm for W_{PLASMA} ($t_{Al}=8$ nm), which is consistent with the values found in the literature.[9,12,32,41] Consequently, the AlO_x surface layer is thicker for natural oxidation, taking into account that the oxidation conditions for both methods were chosen to ensure saturation of the Al oxide growth.[9,12,32,41] λ_{Al} is assumed to be the same in both an AlO_x matrix and a metallic Al one, due to the similarity of their kinetic energies [Fig. 2(a)].

When $\exp[-t_{Al}/(\lambda_{Al}\cos\theta)]$ is not much smaller than 1, i.e., for the thinnest part of the wedge (4 nm), the Nb layer is already detectable even at step 1, and Eq. (3) no longer applies since the upper limit in the integral for $I(Al)$ in Eq. (2) cannot be substituted by ∞. Consequently, the thickness t_{ox} of the AlO_x layer cannot be evaluated from Eq. (4). Equation (3) is now rewritten, following Eq. (2), as

$$R/K=[\exp(t_{ox}/(\lambda_{Al}\cos\theta))-1]\times[1-\exp(-d_{Al}/(\lambda_{Al}\cos\theta))]^{-1}, \quad (5)$$

so that, by taking the value of t_{ox} obtained for the thickest part of the wedge [Eq. (4)], the metallic Al leftover d_{Al} in the thinnest part may be evaluated from Eq. (5), yielding $d_{Al}\approx 3.2$ and 2.2 nm for samples W_{PLASMA} ($t_{Al}=4$ nm) and W_{AIR} ($t_{Al}=4$ nm), respectively. Nevertheless, the values for d_{Al} must be regarded as an order of magnitude since, due to the exponential factor $[1-\exp(-d_{Al}/(\lambda_{Al}\cos\theta))]^{-1}$ in Eq. (5), small variations in the fitted intensities for $I(Al)$ and $I(AlO_x)$ yield large variations in d_{Al}. The estimated value for the thickness of the former Al layer, $t^c_{Al}=t_{ox}/\delta+d_{Al}$, is consistent with the nominal thickness t_{Al} ($t_{Al}=4$ nm; $t^c_{Al}\approx 4.1$ and 4.6 nm for natural and plasma oxidation, respectively), provided the cell expansion δ of the AlO_x layer with respect to the metallic Al layer is considered. The independent calculation of t_{ox} and d_{Al} from Eqs. (4) and (5), respectively, and the fact that these values match the nominal thickness for both oxidation conditions give further support to the relevance of the quantitative XPS analysis of thin oxide layers.

Another calculation of t_{ox} may be gained through the depth profiles in Figs. 4 and 5. Once t_{ox} is determined from the thickest area of the wedge, the sputtering rate (SPR) of the low-energy etching process can be evaluated as $SPR=t_{ox}/t^*$, where t^* is the time for which the oxide layer and the metallic leftover display about the same intensity, i.e., $I(AlO_x)=I(Al)$. t^* is larger for natural oxidation ($\approx$35 s, while $\approx$17 s for plasma oxidation) and leads to SPR $\approx$4.1 nm/min for W_{AIR} ($t_{Al}=8$ nm) and SPR$\approx$6.4 nm/min for W_{PLASMA} ($t_{Al}=8$ nm). Typical values of SPR are about 9.4 nm/min for bulk SiO_2 and 6.5 nm/min for bulk TiO_2.[42]

Downloaded 08 Jun 2010 to 161.116.168.169. Redistribution subject to AIP license or copyright; see http://jap.aip.org/jap/copyright.jsp

In the present article, the etching rate during the first steps depends on both the structure of the AlO_x layer and thickness of the surface contamination layer, the latter also being dependent on the former (see below). As $t^*[W_{AIR}(t_{Al}=4\text{ nm})]\approx t^*[W_{AIR}(t_{Al}=8\text{ nm})]$ and $t^*[W_{PLASMA}(t_{Al}=4\text{ nm})]\approx t^*[W_{PLASMA}(t_{Al}=8\text{ nm})]$ (see Figs. 4 and 5), t_{ox} is thus independent of the former thickness of the Al wedge.

Since intensity I depends quantitatively on concentration C in Eq. (2), Eq. (1) is valid provided all constituents in the sample are homogeneously distributed throughout a depth from the surface much larger than λ. In a multilayered sample, the constituents are not homogeneously distributed, so that Eq. (1) gives an estimate of the atomic fraction as a function of the depth. However, if the thickness t_j of a given layer of an element j is not much larger than λ_j, a better estimate for $C(j)$ is now given by

$$C(j)=[I(j)DF(j)/SF(j)]/[\Sigma_j I(j)DF(j)/SF(j)], \quad (6)$$

where $DF(j)$ is a factor that accounts for photoelectron generation taking place in a finite volume of the sample, and reads

$$DF(j)=1/[1-\exp(-t_j/(\lambda_j\cos\theta))]. \quad (7)$$

Equations (6) and (7) are also qualitatively justified by Eq. (2). Given the nominal thickness of the Nb layer and Al wedge, Eq. (6) leads to results very similar to those shown in Fig. 3(a) [obtained from Eq. (1)].

XPS may also give an estimate of the oxidation state by calculating the O:(oxidize)Al ratio. This ratio is computed in step 2 (after cleaning of the sample surface) for samples W_{AIR}. By taking into account the exponential decay of the XPS signal with thickness in Eq. (2), the O:(oxidize)Al ratio may be expressed as

$$\text{O:(oxidize)Al}=C_O/C_{Al} \quad (8)$$

and

$$C_O\propto I(\text{O})[1-\exp(-t_{ox}/(\lambda_O\cos\theta))]^{-1}/SF_O,$$
$$C_{Al}\propto I(\text{AlO}_x)[1-\exp(-t_{ox}/(\lambda_{Al}\cos\theta))]^{-1}/SF_{Al}, \quad (9)$$

where the proportionality in Eq. (9) results from that in Eq. (2), $SF_O=0.733$ and $SF_{Al}=0.256$ are the sensitivity factors for O 1s and Al 2p, respectively, and $\lambda_O\approx2.3$ nm is the inelastic mean free path for O 1s electrons ($E_B\approx531.0$ eV).[35–36] Equations (8) and (9) give O:(oxidize)Al ≈1.6, 1.8 for W_{AIR} ($t_{Al}=4$ nm) and W_{AIR} ($t_{Al}=8$ nm), respectively, thus suggesting that natural oxidation leads to both AlOOH and Al_2O_3 at the oxide layer. The oxidation state cannot be evaluated in step 1 since the thickness of the surface contamination layer d_c–which gives a further exponential decay of the XPS signal–needs to be known in order to compute O:(oxidize)Al$=[C_O/C_{Al}]A$, with $A=\exp[-d_c/(\lambda_{Al}\cos\theta)]/\exp[-d_c/(\lambda_O\cos\theta)]$, and, even more importantly, the O signal would also be partially related to the surface contamination. It is thus assumed that Eqs. (8) and (9) apply in step 2 after cleaning surface contamination. However, this is not the case for plasma-oxidized samples since the sputtering step (18 s) is already too large ($t^*\sim17$ s) and part of the AlO_x layer has already been etched out in step 2. LeClair *et al.*[14] showed by *in situ* XPS on clean surfaces that plasma-oxidized Co/Al wedge bilayers give the expected O:(oxidize)Al=1.5 value for Al_2O_3. Consequently, Al_2O_3 is taken to calculate K for plasma oxidation in Eqs. (4) and (5), while AlOOH+Al_2O_3 is assumed for natural oxidation.

Native oxides of metals obtained by natural oxidation in air are known to be hydrophillic and porous at the sample surface. O_2 can diffuse easily, which is probably the reason why the oxide layer is thicker than for glow-discharged samples. However, native oxides and suboxides also show poor insulating properties,[43] which precludes the formation of uniform, pinhole-free tunneling barriers. For example, in Nb/NbO_x/Nb tunnel junctions, some of the Nb suboxides show metallic properties and lead to microshorts.[37] Therefore, in most cases the insulating barrier for MTJs does not consist of the native oxide of the FM electrode: plasma oxidation of an intermediate metallic layer is a more reliable technique for high TMR. In addition, native oxides of metals generally form oxide and oxide-hydroxide surface compounds (e.g., AlOOH+Al_2O_3), and a thick surface contamination layer adds to the sample (the more porous, the thicker the surface contamination layer), as seen in Figs. 4 and 5. Here, the intensity in step 1 for natural oxidation is much smaller than in step 2, which is not the case for plasma oxidation. On the contrary, "artificial" oxidation, e.g., glow discharge, leads to a more compact (denser) and thinner surface oxide layer, close to the expected value O:(oxidize)Al $=1.5$,[14] which acts as a passivating layer: as it grows more compact, it avoids further O_2 diffusion. Consequently, the surface layer of contamination is also thinner since the C-C, C-H, and O-H (and many other) groups cannot add to the surface so easily (Fig. 5). As a result, SPR for plasma oxidation is in agreement with the bulk values for the typical oxides (SiO_2 and TiO_2) used for calibrating XPS depth profiles,[42] while SPR for natural oxidation is underestimated due to the surface contamination layer. Therefore, the structure of the oxide layer determines the thickness of the surface contamination layer. This results in higher-sputtering rates during the first steps for plasma oxidation, while the inverse result should be expected since artificial oxidation yields more compact surface oxide layers than the porous native oxides obtained in air (the etching rate of a given compound is inversely proportional to its average density).[35]

Jönsson-Åkerman *et al.* recently showed[32] that $S/I/$FM junctions that display paraboliclike conductance versus dc bias $G(V)$ in the normal state (usual "proof" of tunneling), may show either the Andréev reflection[44,45] (microshorts) or the Bardeen-Cooper-Schrieffer-type density of states (tunnel conduction), at low temperatures. Therefore, the fit of $G(V)$ in the normal state either to the Brinkman-Dynes-Rowell model[46] or to the Simmons' model[47] is not a proof of tunneling and does not rule out the existence of pinholes in the insulating barrier. The typical example of FM/I/S junctions[32] with an insulating barrier displaying pinholes was an Al layer oxidized in air, while plasma-oxidized Al usually resulted in actual pinhole-free tunnel barriers. However, the recent observation of very high MR at room temperature in metallic nanocontacts[26–29] raises the intriguing question of whether conduction through pinholes might actually contribute to MR

Downloaded 08 Jun 2010 to 161.116.168.169. Redistribution subject to AIP license or copyright; see http://jap.aip.org/jap/copyright.jsp

in junctions as much as the tunnel barrier itself.

In conclusion, XPS enables the oxidation state, structure, and thickness of the surface oxide layer, as well as of metallic leftover and sputtering rates in Nb/Al wedge bilayers, to be calculated quantitatively as functions of the oxidation conditions. This is pertinent to research into (magnetic) tunnel junctions.

ACKNOWLEDGMENTS

X.B. is indebted to Dr. J. Portillo and Dr. J. L. Alay (Scientific and Technical Facilities, University of Barcelona) for their technical support during the XPS experiments and for many fruitful discussions of the data. The authors are grateful for financial support from the Spanish CICYT (MAT200-0858) and the Catalan DURSI (ACI2000-04 and 2000SGR00025). Work at UCSD was supported by the U.S. DOE.

[1] T. Miyazaki and N. Tezuka, J. Magn. Magn. Mater. **139**, L231 (1995).
[2] J. S. Moodera, L. R. Kinder, T. M. Wong, and R. Meservey, Phys. Rev. Lett. **74**, 3273 (1995).
[3] J. M. Daughton, J. Appl. Phys. **81**, 3758 (1997).
[4] W. J. Gallagher, S. S. P. Parkin, Y. Lu, X. P. Bian, A. Marley, K. P. Roche, R. A. Altman, S. A. Rishton, C. Jahnes, and T. M. Shaw, J. Appl. Phys. **81**, 3741 (1997).
[5] S. Tehrani, J. M. Slaughter, E. Chen, M. Durlam, J. Shi, and M. DeHerrera, IEEE Trans. Magn. **35**, 2814 (1999).
[6] S. Tehrani, B. Engel, J. M. Slaughter, E. Chen, M. DeHerrera, M. Durlam, P. Naji, R. Whig, J. Janesky, and J. Calder, IEEE Trans. Magn. **36**, 2752 (2000).
[7] J. Zhang, Data Storage **5** (12), 31 (1998).
[8] S. A. Wolf and D. Treger, IEEE Trans. Magn. **36**, 2748 (2000).
[9] S. Cardoso, V. Gehanno, R. Ferreira, and P. P. Freitas, IEEE Trans. Magn. **35**, 2952 (1999).
[10] S. Cardoso, P. P. Freitas, C. de Jesus, P. Wei, and J. C. Soares, Appl. Phys. Lett. **76**, 610 (2000).
[11] S. Cardoso, R. Ferreira, P. P. Freitas, P. Wei, and J. C. Soares, Appl. Phys. Lett. **76**, 3792 (2000).
[12] B. F. P. Roos, P. A. Beck, S. O. Demokritov, B. Hillebrands, and D. Ozkaya, J. Appl. Phys. **89**, 6656 (2001).
[13] M. Weiler, K. Lang, E. Li, and J. Robertson, Appl. Phys. Lett. **72**, 1314 (1998).
[14] P. LeClair, J. T. Kohlhepp, A. A. Smits, H. J. M. Swagten, B. Koopmans, and W. J. M. de Jonge, J. Appl. Phys. **87**, 6070 (2000).
[15] P. Rottländer, H. Kohlstedt, H. A. M. de Gronkel, E. Girgis, J. Schelten, and P. Grünberg, J. Magn. Magn. Mater. **210**, 251 (2000).
[16] P. Rottländer, H. Kohlstedt, P. Grünberg, and E. Girgis, J. Appl. Phys. **87**, 6067 (2000).
[17] J. J. Sun, V. Soares, and P. P. Freitas, Appl. Phys. Lett. **74**, 448 (1999).
[18] S. S. P. Parkin, K. P. Roche, M. G. Samant, P. M. Rice, R. B. Beyers, R. E. Scheuerlein, E. J. O'Sulivan, S. L. Brown, J. Bucchigano, D. W. Abraham, Y. Lu, M. Rooks, P. L. Trouilloud, R. A. Wanner, and W. J. Gallagher, J. Appl. Phys. **85**, 5828 (1999).
[19] Z. Zhang, S. Cardoso, P. P. Freitas, P. Wei, N. Barradas, and J. C. Soares, Appl. Phys. Lett. **78**, 2911 (2001).
[20] Z. Zhang, S. Cardoso, P. P. Freitas, X. Batlle, P. Wei, N. Barradas, and J. C. Soares, J. Appl. Phys. **89**, 6665 (2001).
[21] X. Batlle, P. J. Cuadra, Z. Zhang, S. Cardoso, and P. P. Freitas, *paper DB-09; 41st Annual Magnetism and Magnetic Materials Conference*, Seattle, November, 2001.
[22] J. J. Sun, N. Kasahara, K. Sato, K. Shimazawa, S. Araki, and M. Matsuzaki, J. Appl. Phys. **89**, 6653 (2001).
[23] J. Wang, P. P. Freitas, E. Snoeck, X. Batlle, and J. Cuadra, J. Appl. Phys. (in press); Paper DB-02; *41st Annual Magnetism and Magnetic Materials Conference*, Seattle, November (2001).
[24] C. Prados, B. J. Hattink, E. Pina, X. Batlle, A. Labarta, J. M. González, and A. Hernando, IEEE Trans. Magn. **36**, 2957 (2000).
[25] X. Batlle, B. J. Hattink, A. Labarta, J. J. Åkerman, R. Escudero, and I. K. Schuller (unpublished).
[26] N. García, Appl. Phys. Lett. **77**, 1351 (2000).
[27] N. García, M. Muñoz, and Y.-W. Zhao, Phys. Rev. Lett. **82**, 2923 (1999).
[28] G. Tatara, Y.-W. Zhao, M. Muñoz, and N. García, Phys. Rev. Lett. **83**, 2030 (1999).
[29] N. García, M. Muñoz, and Y.-W. Zhao, Appl. Phys. Lett. **76**, 2586 (2000).
[30] See, for example, *Tunneling Phenomena in Solids*, edited by E. Burnstein and S. Lundqvist (Plenum, New York, 1969).
[31] D. A. Rabson, J. J. Åkerman, A. H. Romero, R. Escudero, C. Leigthon, S. Kim, and I. K. Schuller, J. Appl. Phys. **89**, 2786 (2001).
[32] B. J. Jönsson-Åkerman, R. Escudero, C. Leighton, S. Kim, and I. K. Schuller, Appl. Phys. Lett. **77**, 1870 (2000).
[33] U. Rüdiger, R. Calarco, U. May, K. Samm, J. Hauch, H. Kittur, M. Sperlich, and G. Güntherodt, J. Appl. Phys. **89**, 7573 (2001).
[34] J. J. Åkerman, J. M. Slaughter, R. W. Dave, and I. K. Schuller, Appl. Phys. Lett. **79**, 3104 (2001).
[35] *Practical Surface Analysis*, D. Briggs and M. P. Seah, eds. (Wiley, Chichester, 1983).
[36] *Handbook of X-ray Photoelectron Spectroscopy*, J. Chastain, ed. (Perkin-Elmer Corporation, Eden Prairie, 1992).
[37] See, for example, H. A. M. de Gronckel, H. Kohlstedt, and C. Daniels, Appl. Phys. A: Mater. Sci. Process. **70**, 435 (2000), and references therein.
[38] S. R. Qiu, H.-F. Lai, and J. A. Yarmoff, Phys. Rev. Lett. **85**, 1492 (2000).
[39] J. Kwo, G. K. Wertheim, M. Gurvitch, and D. N. E. Buchanan, Appl. Phys. Lett. **40**, 675 (1982).
[40] Z. G. Zhang, P. P. Freitas, P. J. Cuadra, and X. Batlle (unpublished).
[41] D. Ozkaya, R. E. Dunin-Borkowski, A. K. Petford-Long, P. K. Wong, and M. G. Blamire, J. Appl. Phys. **87**, 5200 (2000).
[42] Electron Spectroscopy for Chemical Analysis Unit, Scientific and Technical Facilities, University of Barcelona (private communication).
[43] J. Halbritter, J. Appl. Phys. **58**, 1320 (1985).
[44] A. F. Andreev, Sov. Phys. JETP **19**, 1228 (1964).
[45] G. E. Blonder, M. Tinkham, and T. M. Klapwijk, Phys. Rev. B **25**, 4515 (1982).
[46] W. F. Brinkman, R. C. Dynes, and J. M. Rowell, J. Appl. Phys. **41**, 1915 (1970).
[47] J. G. Simmons, J. Appl. Phys. **34**, 1793 (1963).

Downloaded 08 Jun 2010 to 161.116.168.169. Redistribution subject to AIP license or copyright; see http://jap.aip.org/jap/copyright.jsp